Computationally Efficient Multirate Continuous Control Set Model Predictive Control With Fast Response for PMSM Drives

Xuesong Wu, *Student Member, IEEE*, Cheng Xue, *Member, IEEE*, Bowei Li, *Graduate Student Member, IEEE*, and Yunwei Li, *Fellow, IEEE*

***Abstract*—Multirate continuous control set model predictive control (CCS-MPC) facilitates higher switching frequencies by simultaneously optimizing control actions across multiple sub-cycles. However, conventional schemes do not incorporate voltage constraints during the optimization process. Consequently, when the commanded voltage exceeds the converter's output capability, output scaling becomes necessary. This not only compromises the performance of the current sub-cycle, but also degrades the tracking accuracy of subsequent sub-cycles, inevitably impairing the system's dynamic performance. Moreover, high-dimensional matrix computations inherent to these schemes present substantial challenges for real-time implementation on cost-effective digital controllers. To overcome these limitations, this article proposes a computationally efficient multirate CCS-MPC scheme with integrated overmodulation capability. The entire tracking process of these sub-cycles is strategically divided into three stages–chasing, transition, and maintaining–each targeting specific control objectives. By doing so, the original large-scale optimization is decomposed into three smaller subproblems, significantly reducing computational complexity. Specifically, the chasing stage incorporates dynamic overmodulation designed based on the shortest feasible path of flux linkage tracking to ensure rapid dynamic response, while in the maintaining stage, the rotor-movement effect across sub-cycles is accounted for, enhancing steady-state performance. Ultimately, experimental results validate the effectiveness of the proposed approach, demonstrating a fivefold improvement in dynamic response and a 62.8% reduction in total execution time.**

***Index Terms*—Continuous control set (CCS), dynamic performance, execution time, model predictive control (MPC), over-modulation, permanent magnet synchronous motor (PMSM), sampling frequency, switching frequency.**

I. Introduction

IN MOTOR drive applications, model predictive control (MPC) has emerged as a promising alternative to traditional control schemes [1], [2], such as field-oriented control (FOC) and direct torque control (DTC). MPC schemes outperform these traditional schemes in both steady-state and dynamic performance. More importantly, MPC schemes can incorporate system constraints and nonlinear factors effectively, enabling multiobjective optimization [3], [4].

MPC can be broadly grouped into two main categories, finite control set MPC (FCS-MPC) and continuous control set MPC (CCS-MPC). In FCS-MPC schemes, feasible switching states are enumerated during each control cycle, and the switching state that minimizes cost function is directly applied to the converter in the subsequent switching cycle. Owing to its intuitive concept and simple structure, FCS-MPC scheme has become the most popular MPC approach in motor drive applications [5], [6], [7].

However, FCS-MPC inherently suffers from an unfixed switching frequency. The absence of a modulation stage results in a dispersed harmonic spectrum, leading to increased iron and copper losses. Consequently, the CCS-MPC has attracted growing attention due to its ability to maintain a fixed switching frequency [8]. In motor drive applications, particularly for systems requiring high power density and low stator current ripple, higher switching frequencies are often essential [9]. In addition, applications with machines that have small stator inductance or operate at high-speed particularly require higher switching frequencies to effectively suppress stator current ripple [10]. The rapid development of wide band-gap (WBG) semiconductor materials, such as the silicon carbide (SiC) and gallium nitride (GaN) has made such high-frequency operation feasible from a hardware perspective. Nevertheless, significant challenges remain on the software side, particularly within the digital controller. In traditional CCS-MPC, the sampling frequency is typically the same as switching frequency or twice its value, and the optimization problem can be solved online using quadratic programming solvers. However, the online optimization typically requires several tens of microseconds [11], posing a bottleneck for adopting higher sampling frequencies to achieve higher switching frequencies.

To simplify the optimization process of CCS-MPC, many researchers have proposed effective approaches. In [12], the possible combinations of switching sequences are reduced by considering the motor dynamic, resulting in only six candidate sequences that need to be evaluated. In [11], the optimal output voltage is obtained using a geometrical method, which avoids the

Received 30 June 2025; revised 20 September 2025; accepted 18 October 2025. Date of publication 23 October 2025; date of current version 19 January 2026. This work was supported by the Natural Sciences and Engineering Research Council (NSERC) of Canada. Recommended for publication by Associate Editor P. Karamanakos. *(Corresponding author: Cheng Xue.)*

Xuesong Wu, Bowei Li, and Yunwei Li are with the Department of Electrical and Computer Engineering, University of Alberta, Edmonton, AB T6G 2R3, Canada (e-mail: xuesong3@ualberta.ca; bli4@ualberta.ca; yunwei.li@ualberta.ca).

Cheng Xue is with the School of Integrated Circuits Science and Engineering, Southwest Jiaotong University, Chengdu 611756, China (e-mail: swjtu_xc@ieee.org).

Color versions of one or more figures in this article are available at https://doi.org/10.1109/TPEL.2025.3624707.

Digital Object Identifier 10.1109/TPEL.2025.3624707

use of general quadratic programming solver. However, in these schemes, the switching frequency remains directly dependent on the sampling frequency, and shortening the sampling interval is the only way to increase the switching frequency. Unfortunately, shortening the sampling interval is not always feasible in practical applications, as the minimum sampling interval is constrained by the total execution time, which also tasks such as analog-to-digital conversion (ADC), speed and rotor position estimation, and communication [13].

To achieve a higher switching frequency under a relatively low sampling frequency, the concept of multirate framework was proposed [14], [15], in which multiple switching cycles are inserted within a single sampling interval. Under this framework, a sequence of voltage vectors, rather than a single voltage converter, is generated as the controller output. This approach effectively reduces the ratio of total execution time and interrupt interval, enabling the implementation of higher switching frequency without the need to upgrade digital controller hardware.

In the multirate scheme, the determination of the optimized sequence is critical, as it directly influences control performance. In [14], the optimized sequence is selected based on a pre-established dataset. However, in motor drive application, the data collection process is extremely complex due to the wide speed range and different operating conditions. As an alternative, a model-based solution employing a lifting model was presented in [15]. Theoretically, the proposed control law enables all sub-cycles to accurately track their references. Nevertheless, two major challenges remain. First, this control law can only be implemented on a limited range of control platforms, as the solving process involves intensive matrix operations, including matrix inversion and high-dimensional matrix multiplication. With the number of sub-cycles increases, solving for the optimized sequence becomes even more challenging, particularly on common commercial digital signal processors (DSPs). Second, system constraints are not explicitly considered during the solving process, which may lead to infeasible voltage vectors. In addition, the scheme loses the ability to perform overmodulation, thereby degrading the system's dynamic performance.

Dynamic performance is a critical criterion in evaluating motor drive systems, and the transient process is directly influenced by inverter output. When a large reference step occurs, the controller might command a relatively large voltage reference, which is beyond the output capability of inverter. In such cases, overmodulation techniques are necessary to improve dc-link voltage utilization ratio and enable fast tracking [16]. To enhance transient performance while keeping the calculation complexity at bay, a geometric approach is proposed in [17], where the current reference is used to identify overmodulation zones and calculate duty cycles. To enhance the current control performance within the overmodulation zone, an optimized current reference is obtained by locating the crossing point between feasible current hexagon boundary and the expected current trajectory [18]. By more finely dividing the voltage vector space, voltage jumps in the high-speed region can be suppressed, and ripple current can also be mitigated [19]. Other objectives, such as common-mode voltage suppression [20] and current distortion reduction [21], can also be incorporated into overmodulation schemes.

In [22], a detailed analysis of the range of time-optimal solutions is carried out based on flux trajectories, and an enhanced overmodulation scheme is developed by introducing a leading angle to the reference voltage vector. This approach effectively mitigates current overshoot while preserving a fast dynamic response. However, it does not guarantee the minimum settling time. In the overmodulation region, the tracking process typically spans multiple switching cycles, making it challenging to determine the optimal voltage vector based solely on information from the current switching cycle [23]. Moreover, the effect of applied voltage vectors on current tracking varies with the rotor position, requiring tracking behavior to be predicted over an extended time horizon. These challenges hint at the potentiality of a multirate structure, in which a sequence of voltage vectors is generated—offering the flexibility to naturally optimize the trajectory.

Currently, most overmodulation techniques are developed for single rate schemes, leaving significant potential to enhance dynamic response performance within multirate CCS-MPC frameworks. To fully leverage the benefits of a multirate structure, the control scheme must not only achieve superior dynamic and steady-state performance but also remain computationally efficient; otherwise, the advantages of the multirate approach are compromised. To address this gap, this work proposes an effective and simple solution of multirate CCS-MPC. The contribution of this work can be summarized as follows.

1) The inverter output constraint is explicitly incorporated into the optimization process. Unlike existing schemes that apply postscaling to unsuitable voltage commands, the proposed approach integrates overmodulation directly into the solving process, thereby preventing the propagation of large tracking errors across sub-cycles.
2) The proposed scheme offers a simple and efficient solution strategy. Instead of solving a high-dimensional sequence of voltage vectors, it decomposes the problem into three smaller sequences, avoiding matrix-heavy computations and simplifying controller design. In addition, the computational complexity increases only marginally with the number of sub-cycles.
3) The proposed scheme exhibits fast dynamic response. The overmodulation voltage vectors are optimized based on the predicted flux linkage trajectory, enabling minimum tracking time.

The rest of this article is organized as follows. Section II describes the system model, while Section III introduces the basic principle of overmodulation and flux tracking. Section IV details the proposed scheme, and then Section V evaluates its performance through experiments. Finally, Section VI concludes this article.

II. System Model

The drive system in Fig. 1(a) consists of a two-level voltage source converter and a permanent magnet synchronous machine (PMSM). The dc-link voltage is denoted by V_{dc}, and the stator current is represented by i_{sx}, where $x \in \{a, b, c\}$ indicates the phase.

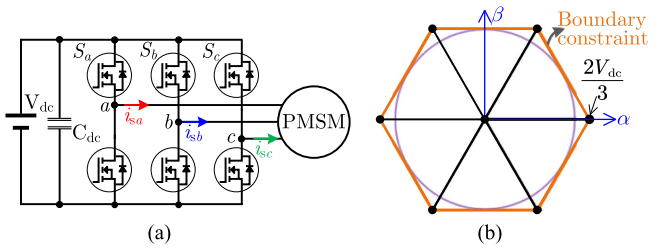

Fig. 1. System topology and inverter output. (a) Topology of a two-level voltage source converter with PMSM. (b) Inverter output voltage vectors in $\alpha\beta$ frame.

A. Inverter Output

For a three-phase two-level converter, its switching state is represented as $(S_a\ S_b\ S_c)$, where $S_x \in \{0, 1\}$. There are eight possible switching states: (0 0 0), (1 0 0), (1 1 0), (0 1 0), (0 1 1), (0 0 1), (1 0 1), and (1 1 1). As illustrated in Fig. 1(b), the maximum output capability is formed by the boundary of a hexagon in $\alpha\beta$ frame.

The converter output voltage in the $\alpha\beta$ reference frame is denoted as $\mathbf{u}_{\alpha\beta} = [u_{s\alpha}\ u_{s\beta}]^{\mathrm{T}}$, and its projection onto the rotating dq reference frame is represented as $\mathbf{u}_{\mathrm{dq}} = [u_{\mathrm{sd}}\ u_{\mathrm{sq}}]^{\mathrm{T}}$. The dq component are obtained using the inverse Park transformation

$$\mathbf{u}_{\mathrm{dq}} = \mathbf{K}_{\mathrm{IP}}(\theta_{\mathrm{e}})\mathbf{u}_{\alpha\beta} = \begin{bmatrix} \cos\theta_{\mathrm{e}} & \sin\theta_{\mathrm{e}} \\ -\sin\theta_{\mathrm{e}} & \cos\theta_{\mathrm{e}} \end{bmatrix} \mathbf{u}_{\alpha\beta} \tag{1}$$

where θ_{e} is the electrical angle.

The voltage vector command is typically provided by the current controller. When the voltage reference remains within the hexagon boundary, full modulation freedom is maintained, and the current controller is not interfered. In addition, the inscribed circle in Fig. 1(b) represents the linear modulation region. However, during rapid current reference change, the commanded voltage vector may exceed the hexagonal limit, requiring the overmodulation techniques to maintain control performance.

B. PMSM Mathematical Model

The variables i_{sd} and i_{sq} represent the stator currents in the dq reference frame. By selecting $\mathbf{i}_{\mathrm{dq}} = [i_{\mathrm{sd}}\ i_{\mathrm{sq}}]^{\mathrm{T}}$ as state variables, the dynamic model of the PMSM in the dq frame can be expressed as

$$\frac{d\mathbf{i}_{\mathrm{dq}}}{dt} = \mathbf{A}\mathbf{i}_{\mathrm{dq}} + \mathbf{B}\mathbf{u}_{\mathrm{dq}} + \mathbf{E} \tag{2}$$

where the input is $\mathbf{u}_{\mathrm{dq}} = [u_{\mathrm{sd}}\ u_{\mathrm{sq}}]^{\mathrm{T}}$, and parametric matrices are defined as

$$\mathbf{A} = \begin{bmatrix} \frac{-R_{\mathrm{s}}}{L_{\mathrm{d}}} & \omega_{\mathrm{e}} \\ -\omega_{\mathrm{e}} & \frac{-R_{\mathrm{s}}}{L_{\mathrm{q}}} \end{bmatrix} \mathbf{B} = \begin{bmatrix} \frac{1}{L_{\mathrm{d}}} & 0 \\ 0 & \frac{1}{L_{\mathrm{q}}} \end{bmatrix} \mathbf{E} = \begin{bmatrix} 0 \\ \frac{-\omega_{\mathrm{e}}\varphi_{\mathrm{f}}}{L_{\mathrm{q}}} \end{bmatrix} \tag{3}$$

where R_{s} is the stator resistance, φ_{f} denotes the permanent magnet flux linkage, L_{d} and L_{q} correspond to the stator inductance in d- and q-axis, respectively, and ω_e is the electrical angular velocity.

Then, the corresponding discrete-time state-space model is expressed as

$$\mathbf{i}_{\mathrm{dq}}(k+1) = \mathbf{A}_{\mathrm{d}}\mathbf{i}_{\mathrm{dq}}(k) + \mathbf{B}_{\mathrm{d}}\mathbf{u}_{\mathrm{dq}}(k) + \mathbf{E}_{\mathrm{d}}. \tag{4}$$

where T_{s} is the sampling period, and k and $k+1$ denote the current and next discrete time steps, respectively, with the discrete-time matrices $\mathbf{A}_{\mathrm{d}}$, $\mathbf{B}_{\mathrm{d}}$ and $\mathbf{E}_{\mathrm{d}}$ are computed as

$$\mathbf{A}_{\mathrm{d}} = e^{\mathbf{A}T_{\mathrm{s}}}, \mathbf{B}_{\mathrm{d}} = \int_0^{T_{\mathrm{s}}} e^{\mathbf{A}\tau}\mathbf{B}\,d\tau, \mathbf{E}_{\mathrm{d}} = \int_0^{T_{\mathrm{s}}} e^{\mathbf{A}\tau}\mathbf{E}\,d\tau. \tag{5}$$

III. Flux Tracking and Dynamic Overmodulation

The closed-loop control of PMSM can be regarded as driving the stator flux linkage to track its reference value through the application of appropriate voltage vectors [23].

A. Flux Tracking

The stator flux linkage can be expressed in terms of stator currents and motor parameters. In the dq frame, the stator flux linkage vector $\boldsymbol{\varphi}_{\mathrm{dq}}$ is given by

$$\boldsymbol{\varphi}_{\mathrm{dq}} = \begin{bmatrix} \varphi_{\mathrm{sd}} \\ \varphi_{\mathrm{sq}} \end{bmatrix} = \begin{bmatrix} L_{\mathrm{d}} & 0 \\ 0 & L_{\mathrm{q}} \end{bmatrix} \mathbf{i}_{\mathrm{dq}} + \begin{bmatrix} \varphi_{\mathrm{f}} \\ 0 \end{bmatrix}. \tag{6}$$

In steady state, both φ_{sd} and φ_{sq} are direct components. The corresponding stator flux linkage in $\alpha\beta$ frame, denoted as $\boldsymbol{\varphi}_{\mathrm{s}} = [\varphi_{\mathrm{s}\alpha}\ \varphi_{\mathrm{s}\beta}]^{\mathrm{T}}$, can be obtained via $\boldsymbol{\varphi}_{\mathrm{s}} = \mathbf{K}_{\mathrm{IP}}^{-1}(\theta_{\mathrm{e}})\boldsymbol{\varphi}_{\mathrm{dq}}$. Similarly, the stator flux reference $\boldsymbol{\varphi}_{\mathrm{s}}^*$ rotates with electrical speed of ω_{e}.

When neglecting the influence of stator resistor, the flux linkage dynamic in $\alpha\beta$ frame can be approximated by

$$\mathbf{u}_{\alpha\beta} = \frac{d}{dt}\boldsymbol{\varphi}_{\mathrm{s}}. \tag{7}$$

Over a short time interval T_{s}, the variation of the stator flux linkage can be approximated by the time integral of $\mathbf{u}_{\alpha\beta}$, i.e.,

$$\boldsymbol{\varphi}_{\mathrm{s}}(k+1) = \boldsymbol{\varphi}_{\mathrm{s}}(k) + \mathbf{u}_{\alpha\beta}(k)T_{\mathrm{s}}. \tag{8}$$

By applying an appropriate voltage vector, both the amplitude and direction of $\boldsymbol{\varphi}_{\mathrm{s}}$ can be adjusted.

Reformulating the current tracking problem to flux tracking problem provides an intuitive method to evaluate the effect of applied voltage vectors in $\alpha\beta$ frame. The flux behavior in $\alpha\beta$ frame is illustrated in Fig. 2. As shown in Fig. 2, within one T_{s}, the change of $\boldsymbol{\varphi}_{\mathrm{s}}$ is determined by the inverter output and time interval, i.e., the $\mathbf{u}_{\alpha\beta}T_{\mathrm{s}}$.

Assuming $\boldsymbol{\varphi}_{\mathrm{s}}(k)$ as the origin, the reachable flux region can be obtained by scaling the voltage hexagon, where the side length of the flux hexagon is $2/3V_{\mathrm{dc}}T_{\mathrm{s}}$. As shown in Fig. 2, the reachable flux references are marked as pentagrams, while these unreachable flux references are marked as diamonds. Since the maximum output capability is a hexagon, the achievable region of flux linkage is also a hexagon.

When the reference vector $\boldsymbol{\varphi}_{\mathrm{s}}^*(k+1)$ lies within this flux hexagon, accurate tracking can be achieved within a single T_{s}. However, if it falls outside this region, the stator flux reference becomes unreachable within one T_{s}, indicating that the tracking process will extend over multiple switching cycles.

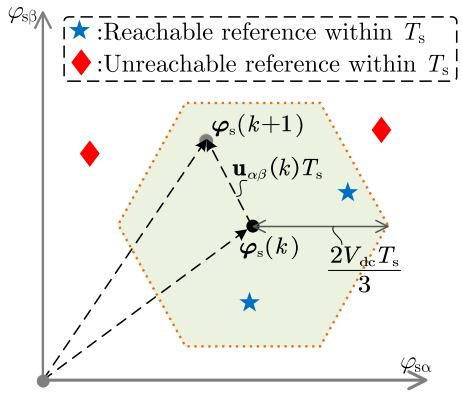

Fig. 2. Flux linkage and and its variation within one T_s in flux $\alpha\beta$ frame.

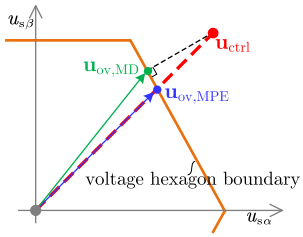

Fig. 3. Various overmodulation schemes.

B. Overmodulation

During transients, the voltage command $\mathbf{u}_{ctrl}$ may exceed the inverter's output limit defined by V_{dc}, as shown in Fig. 3. In such cases, overmodulation techniques are required to clip the voltage vector to the inverter's output hexagon boundary. Several overmodulation strategies have been developed, including the minimum phase error (MPE) method or minimum distance (MD) method. As shown in Fig. 3, if $\mathbf{u}_{ctrl}$ lies outside the voltage hexagon, either $\mathbf{u}_{ov,MPE}$ (calculated using the MPE method) or $\mathbf{u}_{ov,MD}$ (obtained via the MD method) can be applied. The MPE approach determines the intersection point of the desired voltage vector and the hexagon boundary, while the MD approach selects the nearest feasible point on the voltage hexagon.

While the implementation of $\mathbf{u}_{ov,MD}$ and $\mathbf{u}_{ov,MPE}$ do not achieve flux tracking at the end of the current switching cycle, it drives the stator flux toward its reference. The occurrence of overmodulation indicates that the tracking process must span multiple control cycles. In this case, the voltage vector applied during the transient period becomes a sequence of vectors, offering the opportunity for optimization to accelerate the tracking process.

IV. Proposed Multirate CCS-MPC Scheme

Continuous overmodulation extends speed range of motor drives but introduces increased torque ripple and additional acoustic noises [24]. Therefore, in this work, dynamic overmodulation is adopted, meaning that overmodulation is applied only during transient conditions. In steady-state operation, the drive remains within the linear modulation region [22].

Within the multirate framework, a sequence of voltage vectors is generated to guide the stator flux toward its reference. To ensure computational efficiency, the solution process is structured into three distinct operational states: chasing, transition, and maintaining, each tailored to the flux evolution stage during transients.

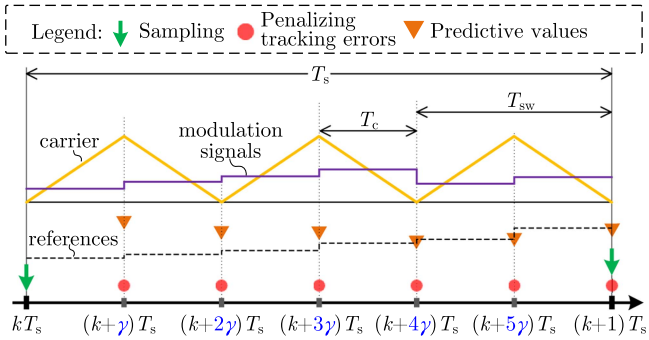

Fig. 4. Structure of multirate framework in the case of $N=6$. Each T_s comprises six T_c, and each T_{sw} spans two T_c.

A. Multirate Framework

In multirate framework, multiple control cycles are inserted into one single sampling cycle. The control interval is denoted as T_c, while the sampling interval is defined as T_s. The multirate parameter N characterizes the relationship between sampling and control intervals, given by

$$T_s = NT_c. \tag{9}$$

The duration of each sub-cycle is defined as γT_s, where $\gamma=1/N$. An example with $N=6$ is illustrated in Fig. 4. To ensure accurate tracking, one switching cycle T_{sw} comprises two control cycles, allowing distinct duty cycle information to be applied to the first and second halves of the switching cycle. An even value of N is preferable in Fig. 4, as it simplifies both the configuration and the triggering of sampling events in practical implementations.

Unlike traditional single rate schemes, the multirate scheme penalizes control errors at all internal instants. As shown in Fig. 4, the tracking errors from instant $(k+\gamma)T_s$, $(k+2\gamma)T_s$, to $(k+1)T_s$, are all considered in the optimization process. It should be noted that the $(k+N\gamma)T_s$ is identical with $(k+1)T_s$.

Consequently, the controller output in multirate scheme is a sequence of voltage vectors, rather than a single voltage vector. These voltage vectors are applied sequentially, each with a duration of T_c. The control output at the sampling instant kT_s is represented as

$$\mathbf{u}_{ctrl}^{k} = \begin{bmatrix}\mathbf{u}_{ctrl}^{1} & \mathbf{u}_{ctrl}^{2} & \cdots & \mathbf{u}_{ctrl}^{N-1} & \mathbf{u}_{ctrl}^{N}\end{bmatrix}. \tag{10}$$

B. References and Tracking Capability

In the $\alpha\beta$ frame, the θ_e evolves at an angular velocity ω_e, causing the stator flux linkage reference to rotate continuously in the flux plane. The flux linkage references for the nth internal sub-cycle is denoted as $\boldsymbol{\varphi}_{s,ref}^{n\gamma}$, where n is an integer less than or equal to N.

Fig. 5 illustrates the evolution of the stator flux reference at different time instants within one T_s. While the amplitude of the flux reference remains constant through the interval, its phase

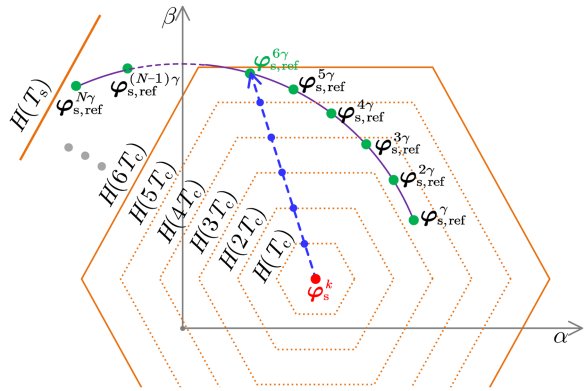

Fig. 5. Reference update and flux tracking capability within internal cycles.

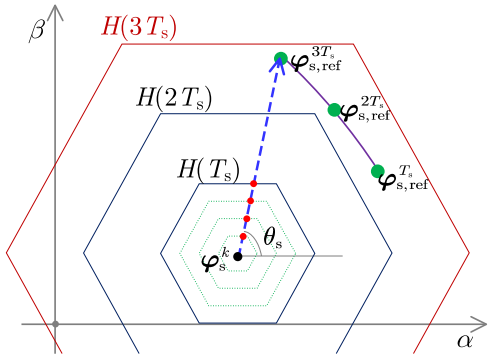

Fig. 6. Determination of output voltage when tracking can not be achieved within one T_s. (Case I).

shifts progressively due to rotor rotation. This dynamic variation poses challenges for flux tracking and output voltage calculation.

To evaluate whether the flux reference is reachable at a given instant, a reachable region function $H(x)$ is defined. Taking the actual stator flux $\boldsymbol{\varphi}_s^k$ being the geometric center, $H(x)$ describes the maximum reachable area within a time interval of x. The boundary of $H(x)$ forms a regular hexagon with $\boldsymbol{\varphi}_s^k$ as the geometric center, and the size of hexagon scales with the duration x. If the distance between $\boldsymbol{\varphi}_s^k$ and $\boldsymbol{\varphi}_{s,ref}^{n\gamma}$ exceeds the range of $H(nT_c)$, then the flux linkage reference is not achievable within nT_c.

In the example shown in Fig. 5, the flux reference remains outside the reachable region during the first five sub-cycles. At the sixth sub-cycle, however, $\boldsymbol{\varphi}_{s,ref}^{6\gamma}$ falls within the hexagonal boundary for the first time, indicating that the flux reference becomes trackable before the end of the sixth control interval.

For the nth sub-cycle, the distance between $\boldsymbol{\varphi}_{s,ref}^{n\gamma}$ and $\boldsymbol{\varphi}_s^k$is defined as $\Delta\boldsymbol{\varphi}_s^{n\gamma}$, with

$$\Delta\boldsymbol{\varphi}_s^{n\gamma} = \boldsymbol{\varphi}_{s,ref}^{n\gamma} - \boldsymbol{\varphi}_s^k = \begin{bmatrix} \Delta\varphi_{s\alpha}^{n\gamma} \\ \Delta\varphi_{s\beta}^{n\gamma} \end{bmatrix}. \tag{11}$$

The flux reference at the nth subcycle is considered reachable if the following hexagonal constraint is satisfied:

$$\begin{bmatrix} \sqrt{3} & 1 \\ 0 & 1 \\ -\sqrt{3} & 1 \\ -\sqrt{3} & -1 \\ 0 & -1 \\ \sqrt{3} & -1 \end{bmatrix} \begin{bmatrix} \Delta\varphi_{s\alpha}^{n\gamma} \\ \Delta\varphi_{s\beta}^{n\gamma} \end{bmatrix} \le \begin{bmatrix} \frac{2V_{dc}nT_c}{\sqrt{3}} \\ \frac{V_{dc}nT_c}{\sqrt{3}} \\ \frac{2V_{dc}nT_c}{\sqrt{3}} \\ \frac{2V_{dc}nT_c}{\sqrt{3}} \\ \frac{V_{dc}nT_c}{\sqrt{3}} \\ \frac{2V_{dc}nT_c}{\sqrt{3}} \end{bmatrix}. \tag{12}$$

As depicted in Fig. 5, the inequality in (12) is not satisfied until the sixth sub-cycle, indicating that the stator flux reference becomes reachable only after five sub-cycles.

C. Proposed Computationally Efficient Solution

When solving for the optimal voltage vector sequence in (10), both the steady state accuracy and transient response should be considered. More specifically, in the presence of a large reference step, dynamic overmodulation is required to enable fast tracking. To this end, it is essential to identify the earliest time instant at which the reference flux becomes reachable and determine the corresponding voltage vector to be applied. Meanwhile, during steady-state operation, the effect of rotor movement across sub-cycles must be accounted for to ensure precise flux tracking.

In some scenarios, the tracking process may span multiple sampling intervals, particularly when the initial tracking error is large. Two representative cases are considered to address this situation:

1) *Case I:* The reference flux cannot be tracked within a single T_s. In this case, all N sub-cycles in the sampling interval operate in the overmodulation region.
2) *Case II:* The reference flux can be successfully tracked within one T_s. Here, the objective is to achieve fast tracking at the first several sub-cycles, and then maintain it in the remaining sub-cycles.

At the first step, the tracking ability is checked with time interval of T_s. If (12) is not satisfied, the solution is calculated using Case I. Otherwise, Case II will be applied. The dedicated solving process for Case I and Case II is detailed as follows.

1) Solution to Case I: The flux linkage at T_s, denoted as $\boldsymbol{\varphi}_{s,ref}^{T_s}$, lies outside the feasible hexagon $H(T_s)$ in this scenario, as illustrated in Fig. 6. This situation requires multiple sampling intervals to bring the flux reference inside the feasible hexagon region. For example, in Fig. 6, the desired stator flux becomes reachable in the third T_s.

Assuming it takes d sampling cycles for the hexagon $H(dT_s)$ to encompass its corresponding stator flux reference $\boldsymbol{\varphi}_{s,ref}^{dT_s}$. By connecting the present flux $\boldsymbol{\varphi}_s^k$ to $\boldsymbol{\varphi}_{s,ref}^{dT_s}$, the slope of flux angle θ_s can be obtained as follows:

$$\tan(\theta_s) = \frac{\varphi_{s\beta,ref}^{dT_s} - \varphi_{s\beta}^k}{\varphi_{s\alpha,ref}^{dT_s} - \varphi_{s\alpha}^k}. \tag{13}$$

It should be noted that the slope calculation is omitted when $\theta_s = \pm 90°$, as the desired voltage can be directly determined in this scenario. In Case I, the prediction horizon for the optimized voltage vector calculation is dT_s.

The angle θ_s defines the desired direction of flux variation and indirectly determines the output voltage vector. In Case I,

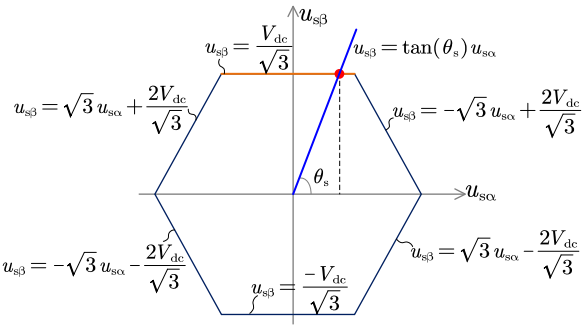

Fig. 7. Boundary equations of hexagon and calculation of the output voltage vector.

TABLE I
OUTPUT VOLTAGE VECTOR UNDER OVERMODULATION

θ_s	$u^n_{ctrl\alpha}$	$u^n_{ctrl\beta}$
$(0,\ \frac{\pi}{3}]$	$\frac{2V_{dc}}{\sqrt{3}\tan(\theta_s)+3}$	$\frac{2V_{dc}\tan(\theta_s)}{\sqrt{3}\tan(\theta_s)+3}$
$(\frac{\pi}{3},\ \frac{2\pi}{3}]$	$\frac{V_{dc}}{\sqrt{3}\tan(\theta_s)}$	$\frac{V_{dc}}{\sqrt{3}}$
$(\frac{2\pi}{3},\ \pi]$	$\frac{2V_{dc}}{\sqrt{3}\tan(\theta_s)-3}$	$\frac{2V_{dc}\tan(\theta_s)}{\sqrt{3}\tan(\theta_s)-3}$
$(-\pi,\ -\frac{2\pi}{3}]$	$\frac{-2V_{dc}}{\sqrt{3}\tan(\theta_s)+3}$	$\frac{-2V_{dc}\tan(\theta_s)}{\sqrt{3}\tan(\theta_s)+3}$
$(-\frac{2\pi}{3},\ -\frac{\pi}{3}]$	$\frac{-V_{dc}}{\sqrt{3}\tan(\theta_s)}$	$\frac{-V_{dc}}{\sqrt{3}}$
$(-\frac{\pi}{3},\ 0]$	$\frac{-2V_{dc}}{\sqrt{3}\tan(\theta_s)-3}$	$\frac{-2V_{dc}\tan(\theta_s)}{\sqrt{3}\tan(\theta_s)-3}$

the same output voltage vector is applied throughout all N sub-cycles of duration T_s. In the $\alpha\beta$ voltage plane, the specific output vector is found as the intersection between the ray at angle θ_s and the boundary of the hexagon. Over-modulation is employed during all N sub-cycles, and the resulting voltage vector for the nth sub-cycle is denoted as $\mathbf{u}^n_{ctrl}=\begin{bmatrix}u^n_{ctrl\alpha} & u^n_{ctrl\beta}\end{bmatrix}^T$. As shown in Fig. 7, the six edges of the hexagon are expressed as six linear equations. The resulting voltage vector at the boundaries can be obtained based on these boundary equations. For example, when $\theta_s\in(\frac{\pi}{3},\ \frac{2\pi}{3}]$, the intersection point is calculated by solving

$$\begin{cases} u^n_{ctrl\beta}=\frac{V_{dc}}{\sqrt{3}} \\ u^n_{ctrl\beta}=\tan(\theta_s)u^n_{ctrl\alpha} \end{cases}. \tag{14}$$

Different hexagon segments are selected depending on the value of θ_s. The corresponding expressions for $\mathbf{u}ctrl^n$ under different angular regions are summarized in Table I. Note that although the reference flux at a future time dTs is used for direction estimation, the computed duty cycle is still applied in the current sampling interval.

As shown in Fig. 6, the stator flux is driven toward its reference along the shortest possible path, thereby ensuring the minimum tracking time. In this scenario, the evaluation of tracking instants is based on time interval of T_s. In practice, if the required d is excessively large, a limit N_{ov} is imposed. In such cases, $\boldsymbol{\varphi}^{N_{ov}T_s}_{s,ref}$ is used to determine θ_s, effectively introducing a lead angle in the output voltage vector.

2) Solution to Case II: When the flux linkage can be tracked within one T_s, the N sub-cycles can generally be divided into three operational stages:

1) *Stage 1:* Chasing with overmodulation. The inverter operates in the overmodulation region to rapidly drive the flux toward its reference.
2) *Stage 2:* Transition with deadbeat control. Deadbeat control is employed to accurately reach the target flux linkage.
3) *Stage 3:* Maintaining under rotor movement. The flux is sustained at the reference under steady-state conditions.

In Case II, a single-step prediction is performed, and N voltage vectors are calculated within one sampling cycle. The first step is to determine the sub-cycle at which the flux linkage becomes trackable. Assume that tracking becomes possible at the mth sub-cycle, the entire sampling interval can then be divided into the three aforementioned stages, as shown in Fig. 8.

a) Stage 1 of Case II: For the first $m-1$ sub-cycles, the output voltage vector lies on the boundary of hexagons, indicating the overmodulation operation. During these sub-cycles, the output voltage is determined by connecting $\boldsymbol{\varphi}^k_s$ and $\boldsymbol{\varphi}^{m\gamma}_{s,ref}$. The detailed voltage components in the $\alpha\beta$ frame for this stage are denoted as $\mathbf{u}_{st1}$ and obtained using the flux angle in Table I. The controller output for stage 1 includes $m-1$ voltage vectors

$$\mathbf{u}^{kT_s}_{st1}=\underbrace{\begin{bmatrix}\mathbf{u}^1_{ctrl} & \mathbf{u}^2_{ctrl} & \cdots & \mathbf{u}^{m-1}_{ctrl}\end{bmatrix}}_{\text{m-1 elements}}. \tag{15}$$

b) Stage 2 of Case II: After the first $m-1$ sub-cycles, the flux linkage is sufficiently close to its reference such that exact tracking is possible in the mth sub-cycle. During the first $m-1$ sub-cycles, identical voltage vectors in the $\alpha\beta$ axes are applied, covering a total duration of $(m-1)\gamma T_s$.

At the end of mth sub-cycle, the stator flux precisely tracks its reference

$$\boldsymbol{\varphi}^{m\gamma}_s=\boldsymbol{\varphi}^{m\gamma}_{s,ref}=\boldsymbol{\varphi}^k_s+\mathbf{u}_{savg}mT_c-R_s\mathbf{i}^k_{s\alpha\beta}mT_c \tag{16}$$

where $\mathbf{u}_{savg}$ is the average voltage vector over the interval from kT_s to $k+mT_c$.

Since the voltage vectors for the first $m-1$ sub-cycles are already known from stage 1

$$\mathbf{u}_{savg}mT_c=\mathbf{u}^1_{ctrl}(m-1)T_c+\mathbf{u}^m_{ctrl}T_c. \tag{17}$$

Thus, the voltage vector for the mth sub-cycle is

$$\mathbf{u}^{kT_s}_{st2}=\mathbf{u}^m_{ctrl}=m\mathbf{u}_{savg}-(m-1)\mathbf{u}^1_{ctrl}. \tag{18}$$

c) Stage 3 of Case II: After completing the chasing and deadbeat tracking in stages 1 and 2, both the flux linkage and dq stator currents reach their corresponding references at instant $(k+m\gamma)T_s$. For the remaining $N-m$ sub-cycles, the control objective is to maintain this tracking. By replacing the predicted stator currents with their reference values in (4), the desired voltage for the nth sub-cycle in the dq frame is

$$\begin{cases} u^n_{dst3}=R_s i_{sd,ref}-\omega_e L_q i_{sq,ref} \\ u^n_{qst3}=R_s i_{sq,ref}+\omega_e(L_d i_{sd,ref}+\varphi_f) \end{cases} \tag{19}$$

where $n\in[m+1,N]$. Notably, the voltage vector in (19) is dc variable and remains valid for all remaining $N-m$ sub-cycles. Considering the rotation of rotor, the electrical angle updates across sub-cycles

$$\theta^{n\gamma}_e=\theta^k_e+\omega_e nT_c. \tag{20}$$

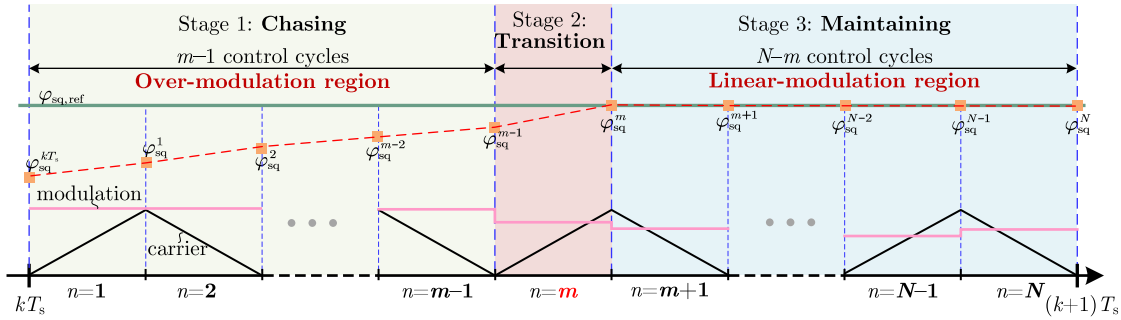

Fig. 8. Three-stage structure when tracking is possible within one sampling interval (Case II).

For the nth sub-cycle, the voltage vector in $\alpha\beta$ frame is expressed as $\mathbf{u}_{\text{ctrl}}^{n}$. By projecting it onto the dq axis over the sub-cycle interval and equating it to $\mathbf{u}_{\text{dqst3}}$, the following expression is obtained [25]:

$$\begin{aligned}\mathbf{u}_{\text{dqst3}} &= \int_{\theta_{\text{e}}^{n\gamma}}^{\theta_{\text{e}}^{n\gamma}+\omega_{\text{e}}T_{\text{c}}} \mathbf{u}_{\text{ctrl}}^{n} e^{-j(\theta_{\text{e}}^{n\gamma}+\omega_{\text{e}}\tau)}\,\mathrm{d}\tau \\ &= \frac{2\sin\frac{\omega_{\text{e}}T_{\text{c}}}{2}}{\omega_{\text{e}}T_{\text{c}}}\mathbf{u}_{\text{ctrl}}^{n} e^{-j\left(\theta_{\text{e}}^{n\gamma}+\frac{\omega_{\text{e}}T_{\text{c}}}{2}\right)} \\ &= \frac{2\sin\frac{\omega_{\text{e}}T_{\text{c}}}{2}}{\omega_{\text{e}}T_{\text{c}}}\mathbf{K}_{\text{IP}}^{-1}\left(\theta_{\text{e}}^{n\gamma}+\frac{\omega_{\text{e}}T_{\text{c}}}{2}\right)\mathbf{u}_{\text{ctrl}}^{n}. \end{aligned} \tag{21}$$

Then, the voltage vector that maintains tracking in the nth sub-cycle is

$$\mathbf{u}_{\text{ctrl}}^{n} = \frac{\omega_{\text{e}}T_{\text{c}}}{2\sin\left(\frac{\omega_{\text{e}}T_{\text{c}}}{2}\right)}\mathbf{K}_{\text{IP}}\left(\theta_{\text{e}}^{n\gamma}+\frac{\omega_{\text{e}}T_{\text{c}}}{2}\right)\mathbf{u}_{\text{dqst3}}^{n}. \tag{22}$$

In (22), the term $\omega_{\text{e}}T_{\text{c}}/2$ is always much smaller than π, as it is constrained by the carrier ratio.

For each sub-cycles in stage 3, the voltage vector information is calculated with corresponding rotor angles. Thus, the output of stage 3 optimization is

$$\mathbf{u}_{\text{st3}}^{kT_{\text{s}}} = \underbrace{\left[\mathbf{u}_{\text{ctrl}}^{m+1} \quad \mathbf{u}_{\text{ctrl}}^{m+2} \quad \cdots \quad \mathbf{u}_{\text{ctrl}}^{N}\right]}_{\text{N-m elements}}. \tag{23}$$

Finally, the complete voltage sequence, which consists of N vectors and is formed by combining the solutions from the three stages, is expressed as

$$\mathbf{u}_{\text{opt}}^{kT_{\text{s}}} = \underbrace{\left[\mathbf{u}_{\text{st1}}^{kT_{\text{s}}} \quad \mathbf{u}_{\text{st2}}^{kT_{\text{s}}} \quad \mathbf{u}_{\text{st3}}^{kT_{\text{s}}}\right]}_{\text{N elements}}. \tag{24}$$

The overall control flowchart of the proposed multirate CCS-MPC scheme is illustrated in Fig. 9. After sampling, delay compensation is performed using the sampled values and the voltage sequence from the previous optimization. Although there are N sub-cycles within each sampling interval, delay compensation is executed only once. Specifically, the average voltage over all N sub-cycles is used, and the compensation is applied over the full sampling period T_{s} rather than the sub-cycle period T_{c}. Subsequently, the system evaluates whether accurate tracking can be achieved within a single sampling interval. If so, the scheme proceeds to Case II, where the N sub-cycles are divided

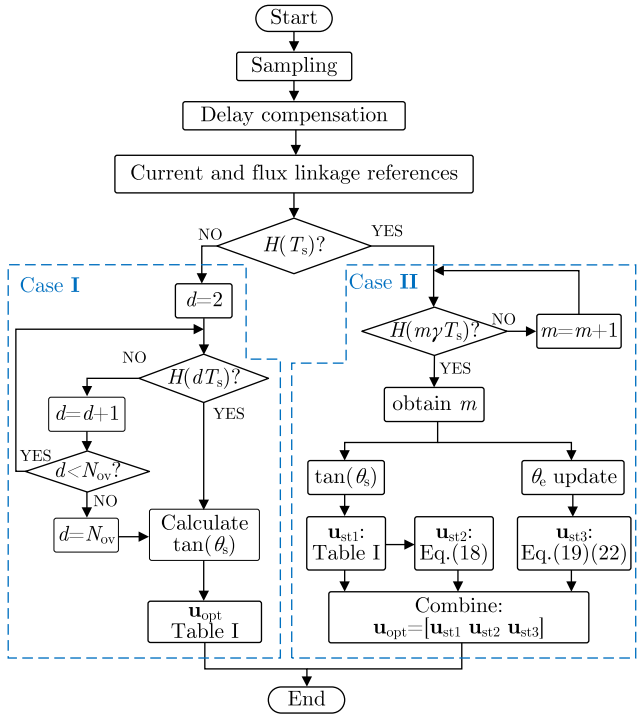

Fig. 9. Flowchart of the proposed multirate CCS-MPC.

into three groups according to the earliest sub-cycle at which accurate tracking becomes feasible. Otherwise, the scheme follows Case I, where an identical voltage vector with overmodulation is applied across all sub-cycles. When considering the influence of dead time, voltage compensation can be performed based on the amplitude and polarity of the load current [26].

V. Experimental Verification

The experimental setup is illustrated in Fig. 10. A dSPACE MicroLabBox is employed as the digital controller. The parameters of the tested PMSM drive are summarized in Table II. An induction machine (IM), mechanically coupled to the PMSM via a shared shaft, is used to provide the load torque. The inverter is powered by a stiff dc source. The converter employs SiC MOSFETS (C3M0065100 K), and the dead time is set to 400 ns.

The proposed multirate (MR) CCS-MPC scheme is evaluated against two existing schemes. The first is the conventional MR

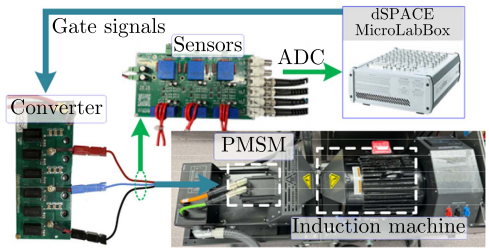

Fig. 10. Experimental setup.

TABLE II
PARAMETERS IN EXPERIMENTS

Parameter	Value	Parameter	Value
DC-link voltage	200 V	Stator resistor	0.8 Ω
Stator inductance	3.1 mH	PM flux	0.151 Wb
Pole pairs	5	Dead time	180 ns
DC-link capacitance	54 μF	Rated current	3.8 A
Rated speed	1000 rpm	Rated load	6 N·m
Sampling frequency	5 kHz	Multirate parameter	$N=10$
Control frequency	50 kHz	Switching frequency	25 kHz

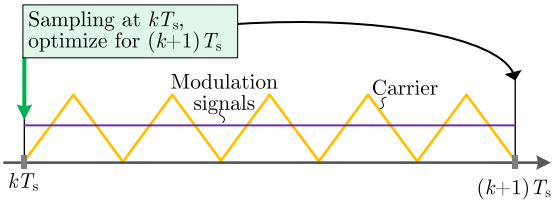

Fig. 11. Sampling and switching pattern of the high-frequency SR CCS-MPC used for experimental comparison.

CCS-MPC from [15] (hereafter referred to as "conventional MR CCS-MPC"). The second is a single-rate (SR) CCS-MPC scheme that operates with a lower sampling/control frequency but a higher switching frequency (hereafter referred to as "high-frequency SR CCS-MPC"). In the high-frequency SR CCS-MPC, multiple switching cycles are embedded within each sampling cycle; however, all sub-cycles share an identical duty cycle [27], as illustrated in Fig. 11. Although the switching frequency differs from the sampling/control frequency, the scheme is still referred to as "single-rate" because the term 'multirate' here only refers to the difference between sampling and control frequencies.

In both the conventional MR CCS-MPC and the high-frequency SR CCS-MPC, when the voltage command exceed the hexagon, the inverter output voltage is clamped to the hexagon using the MPE overmodulation method, as illustrated in Fig. 3.

It should be noted that all three schemes have the same sampling frequency and same switching frequency. The sampling frequency is set to 5 kHz, and 10 sub-cycles are inserted within each sampling interval (i.e., $N=10$). Due to the use of up–down carriers, the effective switching frequency is 25 kHz across all schemes. A key distinction is that the two MR CCS-MPC schemes update the duty cycle information at every sub-cycle, whereas the SR scheme maintains a fixed duty cycle throughout each sampling period.

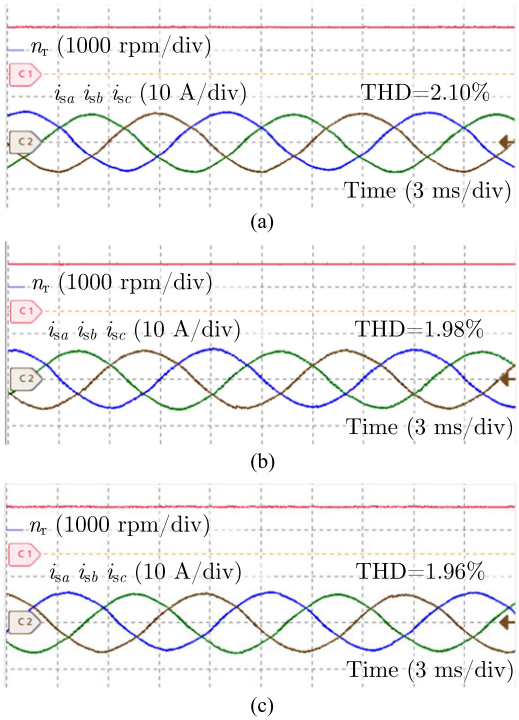

Fig. 12. Experimental results under 1000 r/min rotor speed and 6 N · m load. (a) High-frequency SR CCS-MPC. (b) Conventional MR CCS-MPC. (c) Proposed MR CCS-MPC.

A. Steady-State Performance

The performance under rated speed (1000 r/min) and rated load torque (6 N· m) is illustrated in Fig. 12, where n_r denotes the rotor speed in rpm. Although all schemes operate at the same switching frequency, both the proposed MR scheme and the conventional MR CCS-MPC outperforms the basic high-frequency SR CCS-MPC in terms of stator current quality.

As illustrated in Fig. 12, the total harmonic distortion (THD) in the proposed scheme and the conventional MR CCS-MPC is 1.98% and 1.96%, respectively, both of which are lower than the 2.10% observed in the high-frequency SR CCS-MPC. This improvement is primarily attributed to the updated duty cycles within sub-cycles. In contrast, the traditional scheme applies identical duty cycles across all sub-cycles and fails to account for rotor movement within each switching cycle, leading to degraded current quality. These results also indicate that simply increasing the switching frequency–without updating duty cycle information–cannot take full advantage of high-frequency operation.

B. Dynamic Response Comparison

In the dynamic performance evaluation, the rotor speed is regulated by the IM and only the inner current loop of PMSM is tested. In test, the q-axis current reference of the PMSM steps from 2 to 6 A. To ensure a fair comparison and eliminate the influence of rotor position, this step change is applied at the same rotor angles across all three schemes. The stator current waveforms during the transient are shown in Fig. 13, where i_{amp} represents the amplitude of the stator current vector.

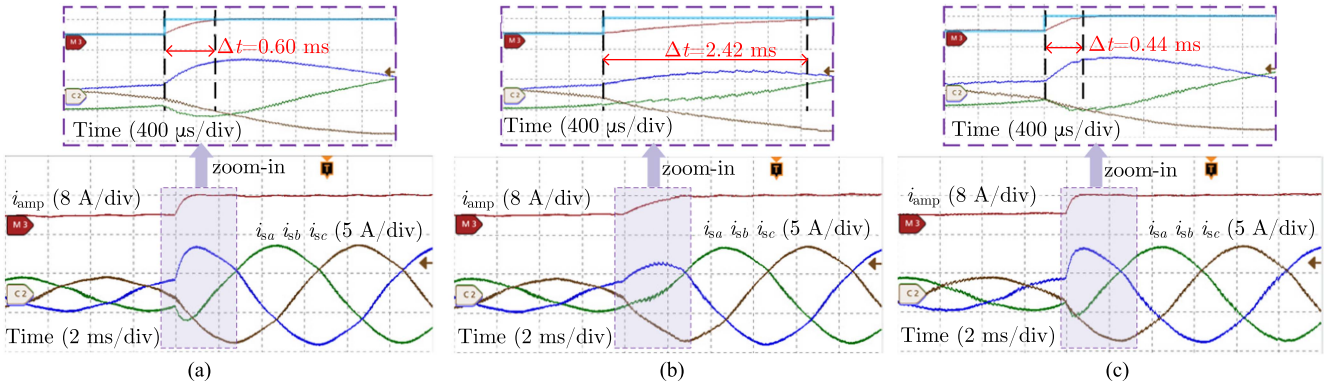

Fig. 13. Experimental results under current step change. (a) High-frequency SR CCS-MPC. (b) Conventional MR CCS-MPC. (c) Proposed MR CCS-MPC.

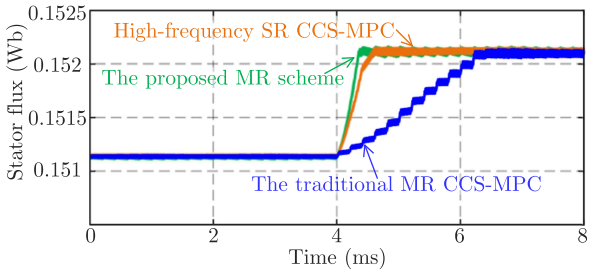

Fig. 14. Stator flux tracking during step change.

As shown in Fig. 13(c), the proposed MR CCS-MPC exhibits the fastest dynamic performance, achieving a settling time of only 0.44 ms, which is more than five times faster than that of the conventional MR CCS-MPC, as shown in Fig. 13(b). The corresponding stator flux amplitudes during the step change are illustrated in Fig. 14.

To gain further insight into controller behavior during transients, the controller output and inverter output voltage vector are illustrated in Fig. 15. Here, t_k denotes the time instant kT_s, at which the transient event is assumed to occur. For both MR CCS-MPC schemes, only the reference voltage vector and inverter output of the first sub-cycle is presented, as the primary difference are most evident in this sub-cycle. In the conventional MR CCS-MPC, the controller attempts to track the reference within the first control cycle, even if the resulting voltage reference is not practically achievable. For the high-frequency SR CCS-MPC, however, all sub-cycles produce identical outputs.

As shown in Fig. 15(a), when the current reference changes, the controller generates a relatively large voltage vector that lies outside the voltage hexagon boundary. Consequently, overmodulation is triggered, and it lasts for two sampling intervals. Then, the voltage vector reenters the hexagon at the instant t_{k+3}. After applying $\mathbf{u}_{inv,k+3}$, the current successfully tracks its reference. Therefore, the total settling time spans three sampling intervals, corresponding to 0.6 ms under a 5 kHz sampling/control frequency.

In Fig. 15(b), it can be found that the controller stays on the overmodulation region for an extended period. The output of controllers is more than 600 V, which exceeds inverter's output capability. It should be noted that only the information about the first sub-cycle is depicted in Fig. 15(b); for the remaining nine cycles, they all located inside the hexagon, as the controller assumes tracking was already completed at the end of first sub-cycle. This will inevitably cause slow dynamic, as only the first sub-cycle contributes to reference tracking. At instant t_{k+13}, the controller's output returns within the hexagon, and after the first control cycle, the tracking is finally completed. This process spans 13 sampling intervals and one control cycle, leading to a total settling time of 2.42 ms. The stator flux linkage during transients is demonstrated in

As shown in Fig. 15(c), the proposed controller maintains its output within the hexagon during transients by considering the voltage constraints in the optimization process. Compared to the traditional scheme, another significant advantage of the proposed method is its ability to perform tracking within internal sub-cycles. In contrast, tracking in the high-frequency SR CCS-MPC scheme is only feasible at the end of full sampling cycles. This advantage becomes even more pronounced with as N increases.

Fig. 16 illustrates the modulation zones associated with each sub-cycle, as well as the exact instant when reference tracking occurs. In the conventional MR CCS-MPC scheme, only the first sub-cycle of each sampling interval enters the overmodulation zone during transients. In contrast, the proposed MR scheme remains in overmodulation zone for two entire sampling intervals and one control cycle, and requires an additional control cycle to complete reference tracking. The entire tracking process spans two sampling intervals and two control cycles, corresponding to 0.44 ms in total.

C. Calculation Burden Assessment

The total execution time and floating-point operatoins of the three schemes are presented in Table III, where additions (Add.), multiplication (Mult.), divisions (Div.), and trigonometric functions (Trig.) are considered.

Compared to the high-frequency SR CCS-MPC scheme, the proposed scheme incurs a slightly higher execution time, as each sub-cycle produces a distinct output, introducing a moderate increase in computational load. However, considering the sampling interval is relatively large at multirate schemes due to its low sampling frequency, this increase is negligible in practice.

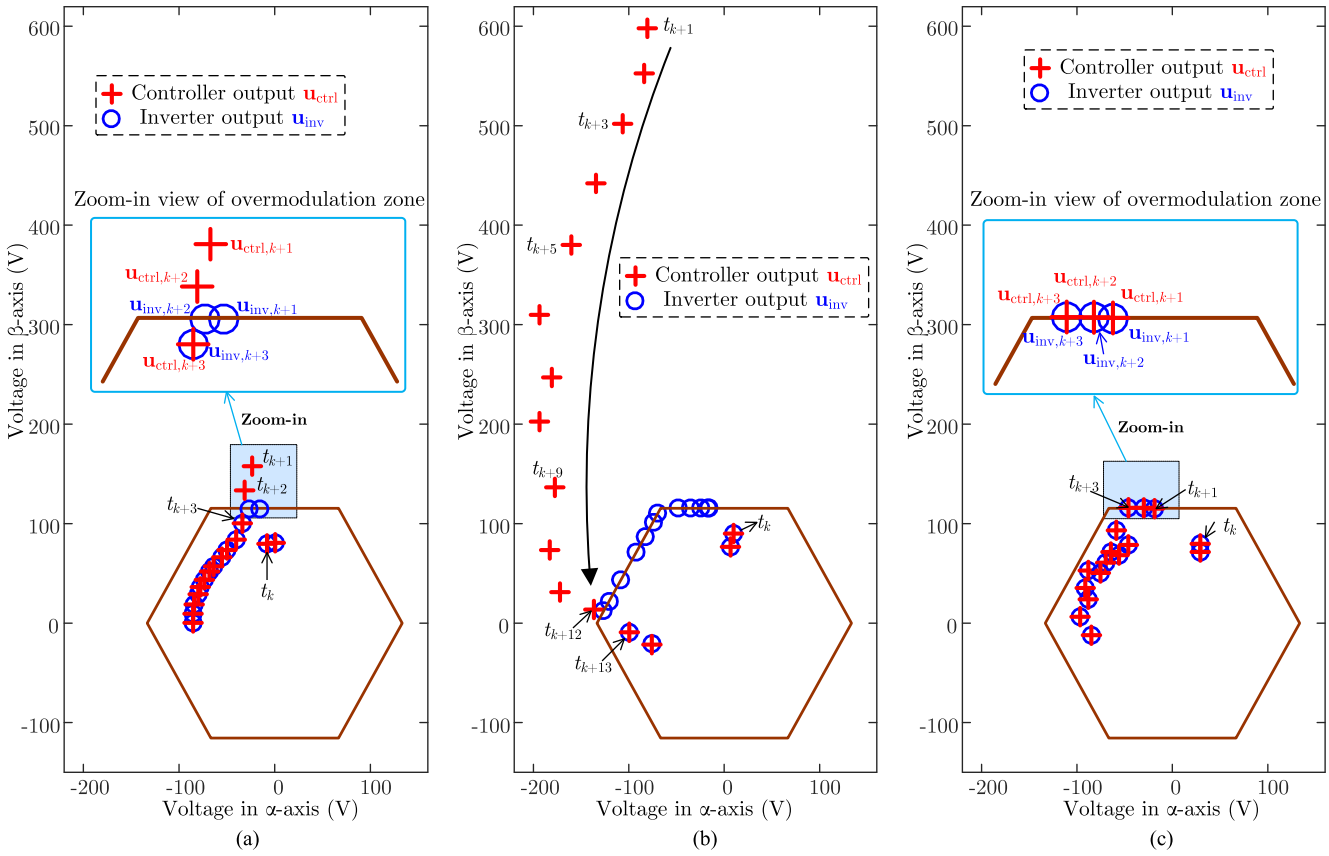

Fig. 15. Controller and inverter output voltages during transients. (a) High-frequency SR CCS-MPC. (b) Conventional MR CCS-MPC. (c) The proposed MR CCS-MPC.

TABLE III
EXECUTION TIME AND FLOATING-POINT OPERATION COMPARISON

Scheme	Execution time (μs)	Add.	Mult.	Div.	Trig.
High-frequency SR CCS-MPC	13.5	28	55	9	4
Conventional MR CCS-MPC	46.8	3770	4077	254	22
Proposed MR CCS-MPC	17.4	188	287	46	26

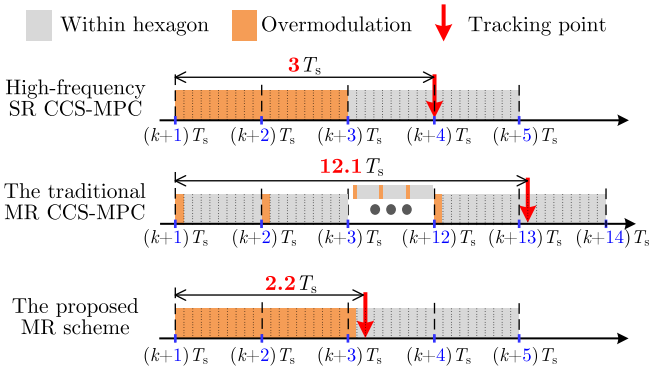

Fig. 16. Modulation zone and tracking point during transients.

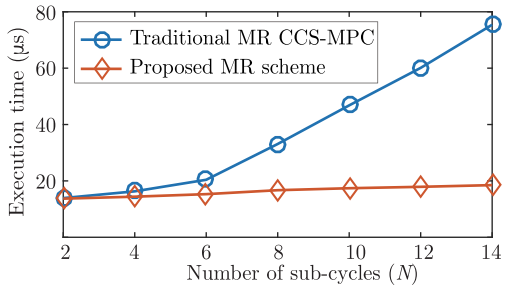

Fig. 17. Total execution time under different N.

In contrast to the conventional MR CCS-MPC scheme, the proposed scheme offers significant advantages in reducing calculation complexity. Specifically, the execution time of the conventional MR CCS-MPC scheme rises to as high as 46.8 μs, whereas the proposed scheme achieves a substantially lower execution time of only 17.4 μs, representing a 62.8% reduction.

In addition, the calculation effort of the conventional MR CCS-MPC increases exponentially with N, as shown in Fig. 17, where the number of sub-cycles grows from 2 to 14. In contrast, the proposed MR CCS-MPC scheme demonstrates only a marginal increase in complexity with respect to N. More

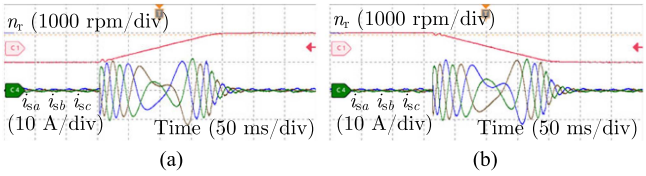

Fig. 18. Speed reversal test under no-load conditions for the proposed MR CCS-MPC. (a) From –500 to 500 r/min. (b) From 500 to –500 r/min.

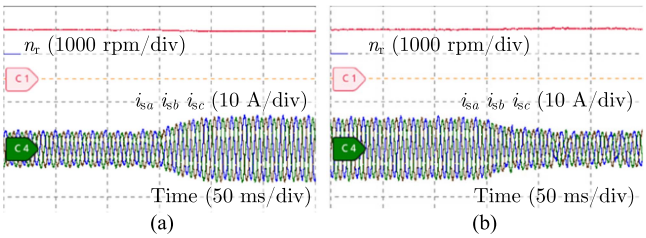

Fig. 19. Load change test at rated speed for the proposed MR CCS-MPC. (a) From 3 to 6 N · m. (b) From 6 to 3 N · m.

TABLE IV
OPTIONS TO ACHIEVE A 25 KHZ SWITCHING FREQUENCY

f_s	N	T_s	Interrupt occupancy
12.5 kHz	4	80 µs	18%
6.25 kHz	8	160 µs	10.44%
5 kHz	10	200 µs	8.70%

importantly, it eliminates the need for complex matrix operations, making it well-suited for implementation on most commercial DSPs.

D. Transient Performance

The experimental results of the speed reversal test for the proposed scheme are presented in Fig. 18, where the speed command of PMSM switches between 500 and −500 r/min under no-load condition.

The experimental results of the load torque change test are shown in Fig. 19, where the load torque switches between 3 and 6 N · m. In this test, speed regulation is implemented in the PMSM side, while the torque change is introduced by modifying the torque output of the IM.

As shown in Figs. 18 and 19, both speed and stator currents are well regulated during transients, with no overshoot observed in the rotor speed. Besides, despite the control of the internal sub-cycles being conducted without intermediate sampling, the proposed scheme demonstrates excellent dynamic performance.

E. Performance Under Different Sub-Cycles and Parameter Mismatch

For a given switching frequency, multiple (f_s, N) combinations are possible. Table IV lists three options that achieve a switching frequency of 25 kHz, where the interrupt occupancy is defined as the ratio of total execution time to sampling interval T_s. As shown in Table IV, a higher N is beneficial to reduce the interrupt occupancy, which means a lower-cost digital controller can be used to achieve a certain switching frequency.

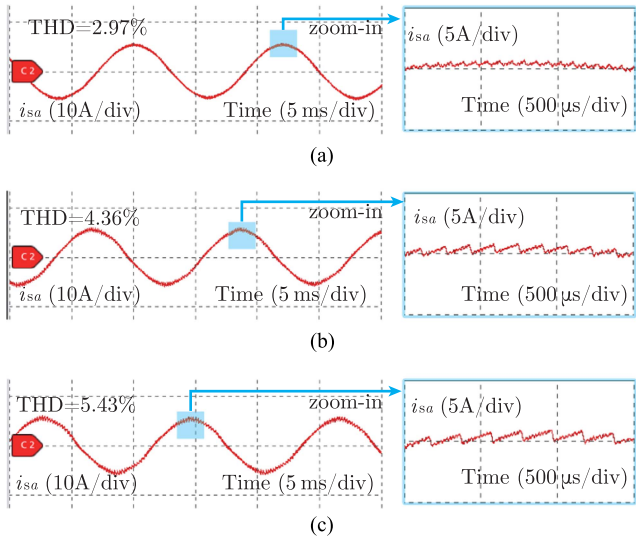

Fig. 20. Performance comparison of the proposed MR scheme under different N and f_s. The rotor flux linkage is overestimated by 20%. (a) $f_s = 12.5$ kHz and $N = 4$. (b) $f_s = 6.25$ kHz and $N = 8$. (c) $f_s = 5$ kHz and $N = 10$.

The performance under parameter mismatch is demonstrated in Fig. 20, where the rotor flux linkage is overestimated by 20%. When $N = 4$, the THD under parameter mismatch is 2.97%, as shown in Fig. 20(a). In comparison, when N is increased to 10, significant distortion appears in the stator current and the THD rises to 5.43% [see Fig. 20(c)]. In addition, the zoomed-in waveforms reveal that the current ripple exhibits a periodicity of T_s, as shown in Fig. 20(b) and (c). Within multirate framework, only the first sub-cycle uses sampled values, while the subsequent sub-cycles rely on predictive results. The current ripple arises from prediction errors will increase and accumulate until the next sampling event occurs. To mitigate the influence of parameter mismatch, parameters identification algorithm can be integrated [28].

From a robustness perspective, a smaller N and higher f_s are preferred. The specific choice of N can be determined based on the interrupt occupancy of digital controller and the desired switching frequency.

VI. CONCLUSION

Conventional multirate CCS-MPC suffers from limited dynamic performance and involves extensive high-dimensional matrix computations, which hinder its deployment on low-cost digital controllers. This paper presents a computationally efficient multirate CCS-MPC scheme that significantly improves dynamic performance. By evaluating the flux linkage tracking capability over a specified time interval, the proposed approach identifies the exact sub-cycle where accurate tracking can be achieved. The entire control process is then divided into three stages, each with distinct objectives, effectively transforming the problem of determining a long voltage vector sequence into solving three smaller sub-sequences. This decomposition simplifies the optimization process and results in a 62.8% reduction in total execution time. Unlike conventional approaches, the proposed scheme exhibits only a minor increase in computational complexity as the number of sub-cycles increases, making it

well-suited for high-frequency applications with limited processing resources. Furthermore, the voltage vector in the overmodulation region is selected based on the principle of minimum tracking distance, ensuring a much faster dynamic response. Experimental results confirm that the proposed method achieves a fivefold improvement in dynamic performance compared to existing multirate CCS-MPC schemes, while maintaining low computational burden suitable for practical implementation.

REFERENCES

[1] S. Kouro, P. Cortes, R. Vargas, U. Ammann, and J. Rodriguez, "Model predictive control–A simple and powerful method to control power converters," *IEEE Trans. Ind. Electron.*, vol. 56, no. 6, pp. 1826–1838, Jun. 2009.

[2] J. Rodriguez et al., "Latest advances of model predictive control in electrical drives–Part II: Applications and benchmarking with classical control methods," *IEEE Trans. Power Electron.*, vol. 37, no. 5, pp. 5047–5061, May 2022.

[3] A. Andersson and T. Thiringer, "Assessment of an improved finite control set model predictive current controller for automotive propulsion applications," *IEEE Trans. Ind. Electron.*, vol. 67, no. 1, pp. 91–100, Jan. 2020.

[4] Y. Wang, Y. Zhang, H. Yang, and J. Rodriguez, "Variable-vector-based model predictive control with reduced current harmonic and controllable switching frequency for PMSM drives," *IEEE Trans. Power Electron.*, vol. 39, no. 12, pp. 16429–16441, Dec. 2024.

[5] P. Karamanakos and T. Geyer, "Guidelines for the design of finite control set model predictive controllers," *IEEE Trans. Power Electron.*, vol. 35, no. 7, pp. 7434–7450, Jul. 2020.

[6] H. Kawai, Z. Zhang, R. Kennel, and S. Doki, "Direct speed control based on finite control set model predictive control with voltage smoother," *IEEE Trans. Ind. Electron.*, vol. 70, no. 3, pp. 2363–2372, Mar. 2023.

[7] H. Xie, F. Wang, Q. Xun, Y. He, J. Rodrıǵuez, and R. Kennel, "A low-complexity gradient descent solution with backtracking iteration approach for finite control set predictive current control," *IEEE Trans. Ind. Electron.*, vol. 69, no. 5, pp. 4522–4533, May 2022.

[8] Q. Yang et al., "Computationally efficient fixed switching frequency direct model predictive control," *IEEE Trans. Power Electron.*, vol. 37, no. 3, pp. 2761–2777, Mar. 2022.

[9] A. K. Morya et al., "Wide bandgap devices in AC electric drives: Opportunities and challenges," *IEEE Trans. Transport. Electrific.*, vol. 5, no. 1, pp. 3–20, Mar. 2019.

[10] A. Aboelhassan, S. Wang, Y. Mikhaylov, G. Buticchi, M. Galea, and S. Bozhko, "Discontinuous modulated model predictive control for low inductance high-speed electric drive applications," *IEEE Trans. Ind. Electron.*, vol. 71, no. 7, pp. 6689–6698, Jul. 2024.

[11] W. Tian et al., "Fast indirect model predictive control for variable speed drives," *IEEE Trans. Power Electron.*, vol. 38, no. 11, pp. 14475–14491, Nov. 2023.

[12] Q. Yang et al., "A fixed switching frequency direct model predictive control for neutral-point-clamped three-level inverters with induction machines," *IEEE Trans. Power Electron.*, vol. 38, no. 11, pp. 13703–13716, Nov. 2023.

[13] Z. Lin, R. Liu, and Y. R. Li, "Transient stability analysis and coordinated phase control method for multiparallel PLL-synchronized inverters during grid fault," *IEEE Trans. Power Electron.*, vol. 40, no. 8, pp. 11442–11451, Aug. 2025.

[14] J. G. Ordonez, P. Montero-Robina, D. Limon, and F. Gordillo, "Real-time implementation of predictive control in power inverters based on nearest neighbor searching," *IEEE Trans. Power Electron.*, vol. 39, no. 1, pp. 384–397, Jan. 2024.

[15] C. Xue, L. Ding, Z. Quan, and Y. Li, "Multirate modeling and predictive control for WBG-device-based high-switching-frequency power converters," *IEEE Trans. Ind. Electron.*, vol. 71, no. 1, pp. 93–103, Jan. 2024.

[16] S. Bolognani and M. Zigliotto, "Novel digital continuous control of SVM inverters in the overmodulation range," *IEEE Trans. Ind. Appl.*, vol. 33, no. 2, pp. 525–530, Mar./Apr. 1997.

[17] A. Sarajian et al., "Overmodulation methods for modulated model predictive control and space vector modulation," *IEEE Trans. Power Electron.*, vol. 36, no. 4, pp. 4549–4559, Apr. 2021.

[18] Z. Jin, W. Xu, J. Wang, and T. Xu, "Dynamic current trajectory tracking strategy with optimized overmodulation method for permanent magnet synchronous motor drives," *IEEE Trans. Ind. Appl.*, vol. 60, no. 6, pp. 8867–8877, Nov./Dec. 2024.

[19] R. Jing, G. Zhang, G. Wang, G. Bi, D. Ding, and D. Xu, "An overmodulation strategy based on voltage vector space division for high-speed surface-mounted PMSM drives," *IEEE Trans. Power Electron.*, vol. 37, no. 12, pp. 15370–15381, Dec. 2022.

[20] Z. Ma, H. Niu, X. Zhang, X. Wu, and X. Cai, "Virtual space vector overmodulation strategy for NPC three-level inverters with common-mode voltage suppression," *IEEE Trans. Power Electron.*, vol. 39, no. 6, pp. 6877–6888, Jun. 2024.

[21] M. Medina-Sanchez, A. G. Yepes, O. Lopez, and J. Doval-Gandoy, "A generalized overmodulation strategy with minimum current distortion for symmetrical and asymmetrical multiphase induction motor drives," *IEEE Trans. Power Electron.*, vol. 39, no. 6, pp. 6552–6567, Jun. 2024.

[22] J. Yoo and S.-K. Sul, "Dynamic overmodulation scheme for improved current regulation in PMSM drives," *IEEE Trans. Power Electron.*, vol. 37, no. 6, pp. 7132–7144, Jun. 2022.

[23] W. Wang, M. Du, and K. Wei, "Rapid torque rising of PMSM by directly chasing rotating flux linkage vector," *IEEE Trans. Emerg. Sel. Topics Power Electron.*, vol. 9, no. 4, pp. 4384–4394, Aug. 2021.

[24] Y.-C. Kwon, S. Kim, and S.-K. Sul, "Six-step operation of PMSM with instantaneous current control," *IEEE Trans. Ind. Appl.*, vol. 50, no. 4, pp. 2614–2625, Jul./Aug. 2014.

[25] B.-H. Bae and S.-K. Sul, "A compensation method for time delay of full-digital synchronous frame current regulator of PWM AC drives," *IEEE Trans. Ind. Appl.*, vol. 39, no. 3, pp. 802–810, May/Jun. 2003.

[26] T. Mannen and H. Fujita, "Dead-time compensation method based on current ripple estimation," *IEEE Trans. Power Electron.*, vol. 30, no. 7, pp. 4016–4024, Jul. 2015.

[27] X. Yuan, I. Laird, and S. Walder, "Opportunities, challenges, and potential solutions in the application of fast-switching SiC power devices and converters," *IEEE Trans. Power Electron.*, vol. 36, no. 4, pp. 3925–3945, Apr. 2021.

[28] B. Long, Z. Zhu, W. Yang, K. T. Chong, J. Rodrıǵuez, and J. M. Guerrero, "Gradient descent optimization based parameter identification for FCS-MPC control of LCL-type grid connected converter," *IEEE Trans. Ind. Electron.*, vol. 69, no. 3, pp. 2631–2643, Mar. 2022.

Xuesong Wu (Student Member, IEEE) received the B.Eng. (Yisheng Mao Honors) and M.Sc. degrees in electrical engineering from Southwest Jiaotong University, Chengdu, China, in 2016 and 2019, respectively. He is currently working toward the Ph.D. degree with the Department of Electrical and Computer Engineering, University of Alberta, Edmonton, AB, Canada.

His research interests include electrical machine drives and high power converters.

Cheng Xue (Member, IEEE) received the B.Eng. (Hons.) and M.Sc. degrees in electrical engineering from Southwest Jiaotong University, Chengdu, China, in 2015 and 2018, respectively, and the Ph.D. degree in energy system from the Department of Electrical and Computer Engineering, University of Alberta, Edmonton, AB, Canada, in 2023.

In 2025, he joined the School of Integrated Circuits Science and Engineering, Southwest Jiaotong University, China, as a Faculty Member. His research interests include advanced control, optimization and integration of power electronics converters for Microgrid applications and high-performance ac electrical machine drives.

Dr. Xue was a Postdoctoral Research Fellow with the Department of Electrical and Computer Engineering, University of Alberta, from 2023 to 2025. He was the recipient of the Chinese Government Award for Outstanding Self-Financed Students Abroad in 2020, IEEE Transactions on Power Electronics Outstanding Reviewer Award twice (in 2022 and 2024) and also the 2023 Ph.D. Thesis Talk Award from the IEEE Power Electronics Society. His Ph.D. research was funded by the Alberta Province's Full-Service Innovation Engine "Alberta Innovates" from 2021 to 2022. He was recognized as the Distinguished Reviewer for IEEE Transactions on Industrial Electronics for three consecutive years from 2021 to 2023. He was recognized as World's Top 2% Scientists ranked by Stanford University.

Bowei Li (Graduate Student Member, IEEE) received the B.S. and M.S. degrees in electrical engineering from Shandong University, Jinan, China, in 2017 and 2020, respectively. He is currently working toward the Ph.D. degree in energy system with the Department of Electrical and Computer Engineering, University of Alberta, Edmonton, AB, Canada.

His research interests include topology, control, and power quality of the dc distribution system.

Yunwei (Ryan) Li (Fellow, IEEE) received the B.Sc. degree in electrical engineering from Tianjin University, Tianjin, China, in 2002, and the Ph.D. degree in electrical engineering from Nanyang Technological University, Singapore, in 2006.

In 2005, he was a Visiting Scholar with Aalborg University, Aalborg, Denmark. From 2006 to 2007, he was a Postdoctoral Research Fellow with Toronto Metropolitan University, Toronto, ON, Canada. In 2007, he was with Rockwell Automation Canada before he joined University of Alberta, Canada in the same year. He is currently a Professor with the University of Alberta Senior Engineering Research Chair, and Chair of the Department of Electrical and Computer Engineering. His research interests include distributed generation, microgrid, renewable energy, high power converters, and electric motor drives.

Dr. Li is the Vice President for Products of IEEE Power Electronics Society (PELS) 2022–2026. He was the Editor-in-Chief for IEEE TRANSACTIONS ON POWER ELECTRONICS LETTERS 2019–2023. He was the General Chair of IEEE ENERGY CONVERSION CONGRESS OF EXPOSITION (ECCE) in 2020 for the first ever virtual version during the pandemic. He was the recipient of the Research Excellence Summit Award by the Association of Professional Engineers and Geoscientists of Alberta in 2025, Nagamori Foundation Award in 2022, and the Richard M. Bass Outstanding Young Power Electronics Engineer Award from IEEE PELS in 2013. He is a Fellow of the Canadian Academy of Engineering, and recognized as the Clarivate Highly Cited Researcher.